Applied Physics Letters

RESEARCH ARTICLE | MAY 16 2023

Localized manipulation of spoof surface acoustic skyrmions with deep-subwavelength gradient structures

Wen-Jun Sun; Hong-Wei Wu; Ping Hu; ... et. al

Appl. Phys. Lett. 122, 202201 (2023)
https://doi.org/10.1063/5.0145611

AIP Publishing

Applied Physics Letters ARTICLE pubs.aip.org/aip/apl

Localized manipulation of spoof surface acoustic skyrmions with deep-subwavelength gradient structures

Cite as: Appl. Phys. Lett. **122**, 202201 (2023); doi: 10.1063/5.0145611
Submitted: 7 February 2023 · Accepted: 1 May 2023 ·
Published Online: 16 May 2023

View Online Export Citation CrossMark

Wen-Jun Sun,[1] Hong-Wei Wu,[1,2,3,a)] Ping Hu,[1] Nong Zhou,[1] Xue Chen,[1] Yong-Qiang Yang,[1] and Zong-Qiang Sheng[1]

AFFILIATIONS

[1]School of Mechanics and Photoelectric Physics, Anhui University of Science and Technology, Huainan 232001, China
[2]Institute of Energy, Hefei Comprehensive National Science Center (Anhui Energy Laboratory), Hefei 230031, China
[3]National Laboratory of Solid State Microstructures, Nanjing University, Nanjing 210093, China

[a)]Author to whom correspondence should be addressed: hwwu@aust.edu.cn

ABSTRACT

Skyrmions with stable vector field configurations have produced various derivatives with various topological textures, such as the Néel type, Bloch type, anti-type, and higher-order Néel type. Here, we theoretically and experimentally demonstrate that the vector field configuration of Néel-type skyrmionic modes can be locally manipulated using gradient grooves in a deep-subwavelength three-dimensional multilayer cylindrical structure. We experimentally observe that the skyrmionic modes can be contracted or expanded to manipulate the distribution of the velocity vectors by tuning the groove depth gradient along the structural radius, which is robust against structural deformations and defects. This type of controllable acoustic skyrmion provides new dimensions for advanced sound information processing, transportation, and data storage in compact structures.

Skyrmions are a class of topological quasiparticles with stable three-dimensional (3D) vector-field configurations in the two-dimensional (2D) plane. Since the concept of skyrmions was proposed in the 1960s,[1] it has attracted considerable interest in different fields, such as Bose–Einstein condensation,[2,3] liquid crystals,[4,5] and magnetic materials.[6–9] Particularly, magnetic skyrmions in magnetic materials have been a high-profile research direction and have sprouted various derivatives with different topological textures, such as the Néel type,[10] Bloch type,[11] anti-type and higher-order Néel type,[12,13] even nested multiple skyrmions, such as skyrmionium,[14] bimeron, and bimeronium.[15,16] These skyrmion derivatives have potential applications in magnetic information storage and processing devices. Recently, skyrmions with stable topological properties have attracted considerable research interest in various fields, such as electromagnetic waves,[17,18] acoustic waves,[19] and elastic waves.[20] Electromagnetic waves, as vectoral fields, including electric and magnetic vectoral components, generate various skyrmionic modes for optical information storage and processing. For example, a specially shaped surface plasmonic structure was designed to manipulate evanescent electromagnetic field distribution to form optical skyrmions.[21–23] By comparing with the abundant magnetic skyrmionic derivatives, various optical skyrmions have recently been constructed using different optical materials, such as optical spin skyrmions with an Archimedean geometric structure,[24] optical spin-meron lattices,[25] optical half-skyrmions generated in a liquid-crystal-filled cavity,[26] and optical Stokes skyrmions with tunable topological textures.[27] Recently, localized spoof plasmonic skyrmionic modes have been proposed, supported by a familiar subwavelength space-coiling metastructure, which are inherent eigenmodes leading to multifrequency bands.[28,29]

It is well known that polarization is an inherent property of vector waves, which is routinely used for transverse waves, such as electromagnetic waves or elastic shear waves. Acoustic waves as longitudinal waves have long been recognized as spinless scalar waves. Recently, structured vector acoustic fields with polarization properties have been observed with interference between multiple propagated acoustic waves with different wave vectors in free space[30] or in the evanescent field of a guide mode traveling along a metamaterial waveguide.[31] In this context, acoustic skyrmion configurations can be created by controlling the velocity-field distributions. Based on this, an acoustic metasurface with hexagonal symmetry was proposed to control the velocity field in acoustic waves to realize the skyrmion lattice mode,[19] which was also demonstrated to be controllable and robust. However, because this lattice structure requires a high degree of symmetry, it has strict requirements for external excitation. Furthermore, a skyrmionic lattice with a large area makes it difficult to manipulate the localized distribution of skyrmionic modes. However, the localized manipulation of velocity vectoral fields plays a very important role in controlling acoustic information storage and processing.

In this study, we propose a deep-subwavelength 3D concentric multilayer cylindrical structure with a gradient groove depth to manipulate the distribution of spoof acoustic surface skyrmionic modes. By eigenmode analysis and simulation, we observed that spoof acoustic surface waves (SASWs) propagated along the radial direction and interference induced skyrmionic modes. When tailoring the homogeneous grooves to gradient grooves, the surface waves become inhomogeneous, and the velocity vectoral distributions contract and expand along the radial direction. The experimental results agreed well with our theoretical analysis and numerical simulations. Furthermore, we demonstrated that the manipulated skyrmionic modes are topologically protected against structural deformation and defects. Controllable skyrmionic modes may provide an alternative approach for locally manipulating the vectoral field distributions in acoustic systems for acoustic information processing and storage.

We implemented acoustic skyrmionic modes using a 3D concentric cylinder; a schematic diagram of the structure is shown in Fig. 1(a). The structure details are an outside radius $R = 5$ cm, wall thickness $b = 0.1$ cm, period $d = 0.25$ cm, groove width $a = d - b = 0.15$ cm, structure height $H = 5$ cm, and the number of channels $N = 20$. For a better illustration of the internal structural details, we present a cross-sectional view on the right side of Fig. 1(a). The substrates below the grooves of the structure are indicated by the green region, and the height of the upper groove is indicated by h_n. To design the gradient groove depth expediently, we set two adjacent grooves with the same height, $h_n = h_{n+1}$, (n = 1, 3, 5, …, N-1). The gradient difference Δh in the gradient structure along the radial direction was $\Delta h = h_n - h_{n+2}$. We designed three different types of structures according to the variation of the gradient difference Δh. As shown on the right side of Fig. 1(a), when the gradient difference $\Delta h > 0$, the green regions become high along the radial direction from the center of the structure to the edge, which is referred to as a concave-type structure. We refer to structures with the gradient difference $\Delta h = 0$ and gradient difference $\Delta h < 0$ as flat-type and convex-type structures, respectively.

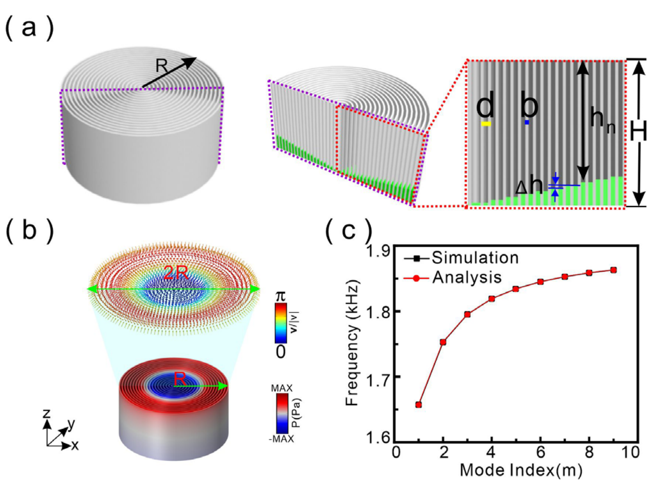

FIG. 1. Schematic structure and simulation results of skyrmionic mode formed by the acoustic velocity field. (a) Left: Schematic diagram of structural unit with structural parameters: outside radius R. Right: Schematic diagram of the section of the structure: the bottom filled part is shown in green, groove height of the channel h_n, channel period d, and wall thickness b, structure height H. (b) Simulation diagram of the skyrmionic mode formed by the acoustic velocity field; the direction of the acoustic velocity field is shown by the arrow. (c) Theoretical calculations and simulations for the frequency of the skyrmionic modes with different mode index.

In Fig. 1(b), as an example, we show the distribution of the acoustic pressure and velocity fields in the first-order Néel-type skyrmionic mode for a flat structure. The colors in the structure represent the pressure field distribution, whereas the arrows above the structure represent the acoustic velocity field vectors distributed on the structure surface. We observe that its acoustic velocity field vector gradually flips from the central "up" state to edge "down" state along the radius direction, which is in accordance with the characteristics of the Néel-type skyrmions.

For the period corrugations along the radial direction, it is well known that the spoof acoustic surface waves are formed and propagated along the radius. The inward and outward spoof acoustic surface waves (SASWs) mutually interfere to induce a standing wave when the Fabry–Pérot (FP) resonating condition is satisfied,[32,33] which can be expressed as

$$k_{\mathrm{SASW}} R = m\pi + \gamma \quad (m = 1, 2, 3\ldots), \tag{1}$$

where k_{SASW} is the wave vector of the spoof acoustic surface waves, R is the outside radius of the structure, m is a positive integer indicating the order of the resonant mode, and γ is the induced phase shift due to the partial reflection at the edge and center of the structure. The spoof acoustic surface waves have the following dispersion relationship:

$$k_{\mathrm{SASW}} = \frac{\omega}{c}\sqrt{1 + \left(\frac{a}{d}\right)^2 \tan\left(\frac{\omega}{c}h_n\right)^2}, \tag{2}$$

where $\omega = 2\pi f$ is the angular frequency. The reflection phase γ at both terminations can be approximately experimentally retrieved from the measured resonant frequency and dispersion relation.[34] For instance, the measured resonant frequency of the first-order skyrmionic mode for the flat-type structure is $f_1 = 1660$ Hz, then $k_{\mathrm{SASW}} R = 1.495\pi$, the reflection phase can be derived as $\gamma = 0.495\pi$. Using a similar method, we derived the eigen-frequencies of the first nine order skyrmionic modes, as shown in Fig. 1(c). The theoretical results (red line) agree with the simulated results (black line) by full-wave simulation based on the commercial software COMSOL Multiphysics with a pressure acoustic module.

Next, we discuss the manipulation of the velocity vector distribution of the skyrmionic modes by tailoring the gradient of the groove depth along the radial direction. It is well known that the topological properties of the skyrmion modes can be characterized by the skyrmion number S:

$$S = \frac{1}{4\pi}\iint \vec{n} \cdot \left(\frac{\partial \vec{n}}{\partial x} \times \frac{\partial \vec{n}}{\partial y}\right) dxdy, \tag{3}$$

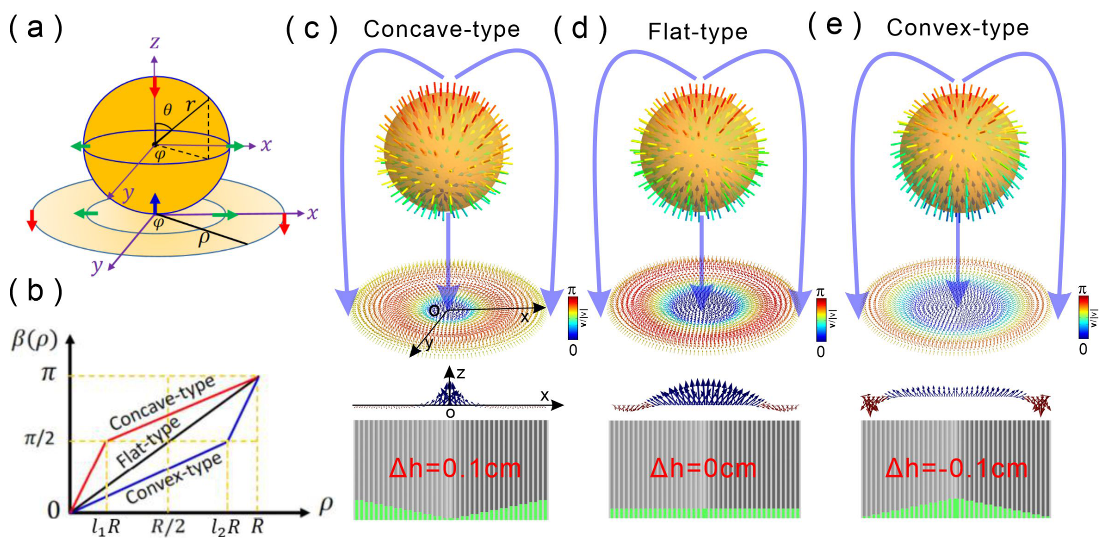

FIG. 2. First-order modes of skyrmion formed by acoustic velocity fields and their theoretical models in different structures. (a) Mapping relations of 3D parametric sphere in 2D velocity vector field. (b) Relation between $\beta(\rho)$ and ρ for the three structural types. (c)–(e) Velocity vector distributions in concave-, flat-, and convex-type structures.

where $\vec{n} = \frac{Re(\vec{v})}{|Re(\vec{v})|}$. In our structure, the acoustic skyrmion number S is represented by the acoustic velocity field $\vec{v}$ using Eq. (3). The 2D velocity field vectors represent the vector distribution on a 3D parameterized sphere by longitude α and latitude β. The mapping relation is shown in Fig. 2(a); here, the 3D coordinated system is (r, θ, φ), whereas the 2D coordinated system is (ρ, φ). The colored arrows represent the velocity vectors distributed on the 2D plane and 3D sphere to present the mapping relation. Therefore, the skyrmion number S can be deduced as

$$S = \left(\frac{1}{2}\int_0^R \sin\beta(\rho)d\rho\right)\left(\frac{1}{2\pi}\int_0^{2\pi}\frac{d\alpha(\varphi)}{d\varphi}d\varphi\right) = p\cdot m, \quad (4)$$

where $p = \frac{1}{2}\left[\cos\beta(\rho)\right]\big|_{\rho=0}^{\rho=R}$ defining the polarity, $m = \frac{1}{2\pi}\left[\alpha(\varphi)\right]\big|_{\varphi=0}^{\varphi=2\pi}$ defining the vorticity. $\beta(\rho) = \pi - \theta(\rho)$, $\alpha(\varphi) = m\varphi$ for the Néel-type skyrmion. In fact, we can maintain the polarity $p = 1$ (i.e., the velocity vectoral arrow at the structure center is upward and downward at the structure edge) while the arrow flip position and distribution can be manipulated by the gradient structures. For the flat-type

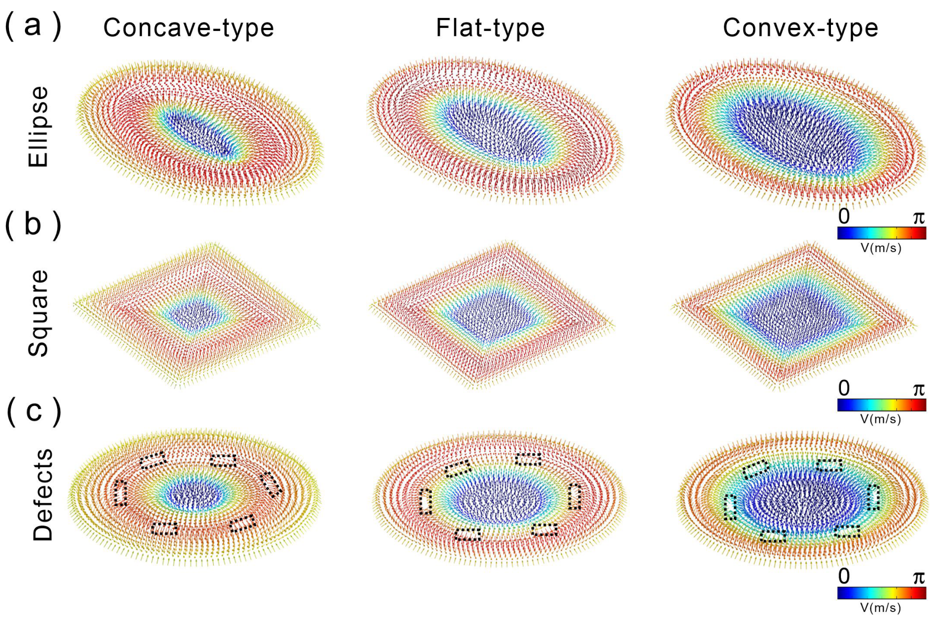

FIG. 3. Skyrmionic modes of structures with deformation/defects. First-order skyrmionic modes generated on the surface of the gradient ellipse structures (a), the gradient square structures (b), and the gradient cylinder structures with the cavity-type defects (c).

structure, the standing wave is a homogenous distribution along the radial direction; the flip point at $\rho = R/2$, and the line relation between β and ρ is $\beta = \frac{\pi}{R}\rho$ as shown by the black line of Fig. 2(b). However, when we tune the groove depth to a concave structure, the deeper grooves have larger wave vectors of the spoof acoustic surface waves, according to Eq. (2) and a stronger confined capability to induce a contracted pattern. The velocity vectors drastically rotate the direction at $0 < \rho < l_1 R$ and gently rotate the direction at $l_1 R < \rho < R$, where $l_1 < 0.5$. The relation between β and ρ is sectionalized as shown by the red lines of Fig. 2(b). Inversely, if the gradient structure is designed as a convex-type structure, the structure edge has a stronger confined capability, and the flip point will be expanded to $\rho = l_2 R$ ($l_2 > 0.5$). The sectionalized relation is indicated by the blue lines. The parameters l_1 *and* l_2 depend on the gradient magnitude Δh.

To demonstrate the manipulation of the skyrmionic modes, Figs. 2(c)–2(e) present the distribution of the first-order Néel-type skyrmions parameterized spheres at the first row for concave-type ($\Delta h = 0.1$cm), flat-type ($\Delta h = 0.0$cm), and convex-type ($\Delta h = -0.1$cm) structures. The second row corresponds to the mapped velocity vectoral distributions for the three structures on the (x, y) plane, and the third row shows the velocity vectoral distributions for the three structures on the (x, z) plane for convenient observation. It is not difficult to observe that the flipped locations of the arrows are gradually extrapolated from concave- to convex-type structures. Observing the parameterized spheres, we deduced that the center of the vectoral arrows distributed on the sphere surface moved up from left to right. These simulation results agree with the discussion in Fig. 2(b). Furthermore, we demonstrate that the degrees of contraction and expansion depend on the gradient degree Δh in Fig. S1 in the supplementary material. A larger gradient degree has a stronger contraction or expansion capability. We also present the high-order skyrmionic mode distributions for the three types of structures in Fig. S2 in the supplementary material.

One unique feature of skyrmionic modes is their inherent topological characteristics. When the geometry deforms, the underlying

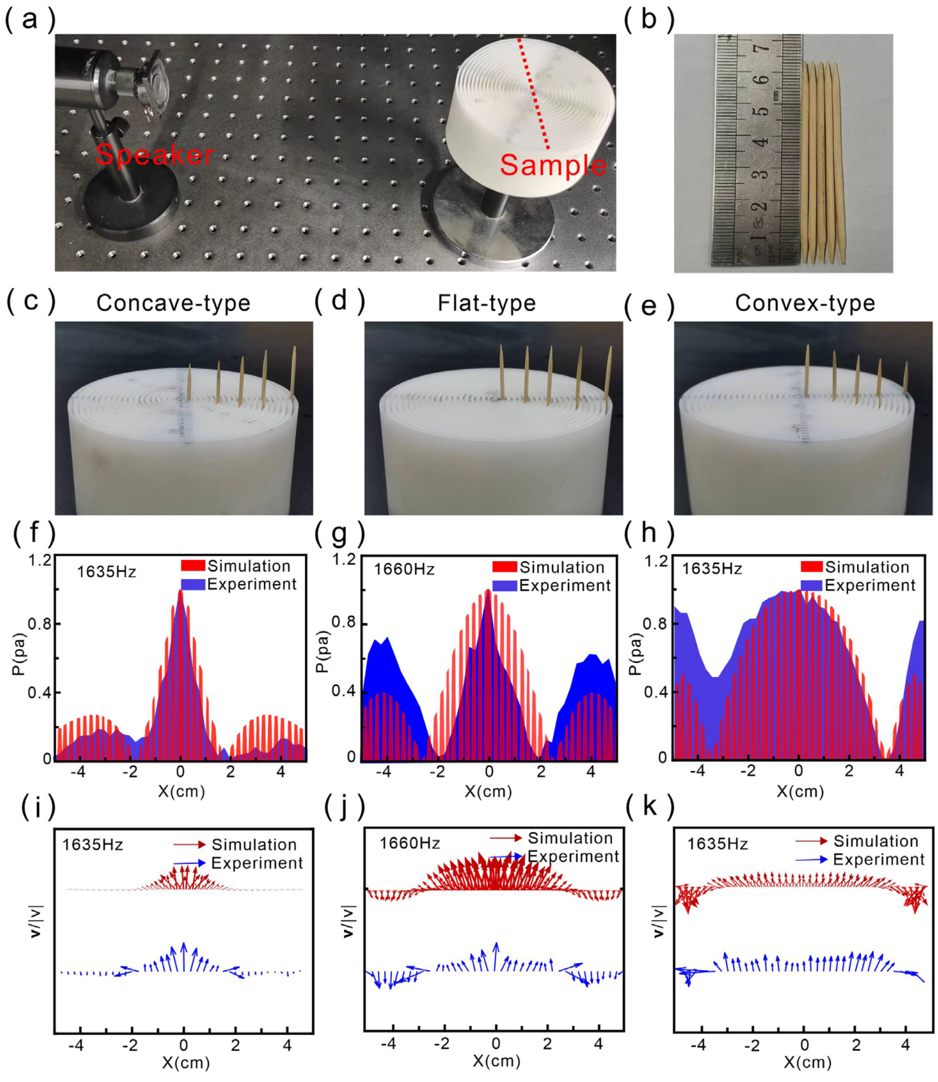

FIG. 4. Experimental measurement of cross-sectional sound pressure field distributions and their sound velocity field distributions. (a) Schematic diagram of the experimental setup. (b) Five equal-length toothpicks. (c)–(e) From left to right: Samples of concave-type structure, flat-type structure, and convex-type structure schematically shown in order. The first-order skyrmionic modes excitation frequency $f = 1635$ Hz, $f = 1660$ Hz, and $f = 1635$ Hz. (f)–(h) Simulated (red) and experimentally measured (blue) cross-sectional sound field distributions on the surface of the sound pressure field for the three structures in the first-order modes, respectively. (i)–(k) Cross-sectional sound velocity field distributions along the red line on the three sample structures for simulated (red arrow) and experimental (blue arrow) first-order skyrmionic modes.

skyrmion-field configuration adapts to the new geometry without affecting the topological junctions. Thus, we transformed the concentric circular structure into elliptical and square structures, as shown in Figs. 3(a) and 3(b), respectively. We found that the first-order skyrmionic mode was robust to structural distortions. Particularly, the localized manipulations of the velocity field distribution in the elliptical and square structures were similar to those in a circular structure. Furthermore, we also investigated the influence of the defects introduced in the isometric concentric circles on the robustness of the skyrmionic mode. We introduced six cavity-type defects in the middle of the concentric circles to disrupt the continuity of their structures. As shown in Fig. 3(c), the first-order skyrmionic modes do not produce large variations compared with the perfect structure for the concave, flat, and convex structures. For high-order skyrmionic modes, the same topological properties are observed in Fig. S3 in the supplementary material. These results demonstrate that controllable skyrmionic modes are robust against structural deformation and defects.

We theoretically analyzed and numerically demonstrated that the spoof localized acoustic surface skyrmionic mode distributions could be freely manipulated on the structural surface. Next, we experimentally observed the velocity vectoral distributions on the surface of the three different types of structures. As shown in Fig. 4(a), we placed the loudspeaker as the point source in front of the sample with 20 cm. To begin the experiment, the sound signal generated in the signal generator (AFG1022, Tektronix) was amplified in a power amplifier (CPA2400, SinoCinetech) to drive the loudspeaker, and measure the sound pressure at each groove surface along the radial direction of the sample, as indicated by the red dashed line. Figures 4(c)–4(e) show samples with concave, flat, and convex structures, respectively. To clearly show the inner gradient structures, we inserted five equal-length toothpicks [Fig. 4(b)] along the radial direction into the three structures. The structure type was indicated by the height of the five toothpicks on the outside of the structure. Figures 4(f)–4(h) show the pressure field distributions of the three structures obtained by experimental measurement (blue area) and simulation (red area) along the structure diameter. The experimental results agree well with the simulated pressure field distributions. Particularly, we found that the nodes of the pressure field were extrapolated along the radial direction from the concave- to convex-type structure. Next, we took the measured sound pressure field distribution to obtain the corresponding acoustic velocity field vector via $\vec{v} = \frac{1}{i\omega\rho_0}\nabla p$, where ω and ρ_0 are the angular frequency and density of air, respectively. Figures 4(i)–4(k) show the experimentally measured (blue arrows) and simulated (red arrows) sound velocity field vectors for the three structures in the first-order skyrmionic modes. The experimental results indicated that the skyrmion modes of the acoustic velocity field can be manipulated with the variation of Δh in gradient structures.

In summary, we theoretically proposed and experimentally demonstrated localized controllable spoof localized acoustic surface skyrmionic modes based on deep subwavelength localized gradient structures. We found that the line relation between the latitude and radius was broken, and the velocity vectoral distributions become inhomogeneous when gradient groove depths were introduced into the structure. The distributions of the skyrmionic modes can be contracted and expanded depending on the degree of the structural gradient. Furthermore, the topological properties of manipulated localized acoustic skyrmionic modes were demonstrated by introducing geometric deformations and defects. Similar structures can be designed with multilayer metallic rings in the microwave range to obtain similar results for optical skyrmions. The tunability and stability of acoustic skyrmionic modes in gradient structures make them promising for rich applications, such as the manipulation of tiny particles and the storage and processing of acoustic information.

See the supplementary material for the effect of structure on skyrmionic modes at different gradient difference Δh; the high-order skyrmionic modes distributions on the three kind structures; and topological properties of higher-order skyrmionic modes for structure deformation and defects.

This work was supported by Major Scientific research projects of colleges and universities in Anhui Province (Grant No. 2022AH040114) and the University Synergy Innovation Program of Anhui Province (Grant No. GXXT-2022-015).

AUTHOR DECLARATIONS

Conflict of Interest

The authors have no conflicts to disclose.

Author Contributions

Wen-Jun Sun: Data curation (equal); Investigation (equal); Writing – original draft (equal). **Hong-Wei Wu:** Conceptualization (equal); Funding acquisition (equal); Investigation (equal); Supervision (equal); Writing – review & editing (equal). **Ping Hu:** Investigation (equal); Writing – original draft (equal). **Nong Zhou:** Investigation (equal); Software (equal); Validation (equal). **Xue Chen:** Supervision (equal); Visualization (equal). **Yong-Qiang Yang:** Supervision (equal); Visualization (equal). **Zong-Qiang Sheng:** Supervision (equal); Visualization (equal).

DATA AVAILABILITY

The data that support the findings of this study are available from the corresponding author upon reasonable request.

REFERENCES

[1] T. H. R. Skyrme, "A unified field theory of mesons and baryons," Nucl. Phys. **31**, 556 (1962).
[2] T. L. Ho, "Spinor Bose condensates in optical traps," Phys. Rev. Lett. **81**, 742 (1998).
[3] U. Al Khawaja and H. Stoof, "Skyrmions in a ferromagnetic Bose–Einstein condensate," Nature **411**, 918 (2001).
[4] D. C. Wright and D. C. Mermin, "Crystalline liquids: The blue phases," Rev. Mod. Phys. **61**, 385 (1989).
[5] J. I. Fukuda and S. Žumer, "Quasi-two-dimensional skyrmion lattices in a chiral nematic liquid crystal," Nat. Commun. **2**, 246 (2011).
[6] B. Göbel, I. Mertig, and O. A. Tretiakov, "Beyond skyrmions: Review and perspectives of alternative magnetic quasiparticles," Phys. Rep. **895**, 1–28 (2021).
[7] Y. Tokura and N. Kanazawa, "Magnetic skyrmion materials," Chem. Rev. **121**, 2857 (2021).
[8] J. L. Chen, J. F. Hu, and H. M. Yu, "Chiral emission of exchange spin waves by magnetic skyrmions," ACS Nano **15**, 4372 (2021).
[9] N. Nagaosa and Y. Tokura, "Topological properties and dynamics of magnetic skyrmions," Nat. Nanotechnol. **8**, 899 (2013).

[10]I. Kézsmárki, S. Bordács, P. Milde, E. Neuber, L. M. Eng, J. S. White, H. M. Rønnow, C. D. Dewhurst, M. Mochizuki, K. Yanai, H. Nakamura, D. Ehlers, V. Tsurkan, and A. Loidl, "Néel-type skyrmion lattice with confined orientation in the polar magnetic semiconductor GaV_4S_8," Nat. Mater. **14**, 1116 (2015).
[11]P. Milde, D. Köhler, J. Seidel, L. M. Eng, A. Bauer, A. Chacon, J. Kindervater, S. Mühlbauer, C. Pfleiderer, S. Buhrandt, C. Schütte, and A. Rosch, "Unwinding of a skyrmion lattice by magnetic monopoles," Science **340**, 1076 (2013).
[12]A. Nayak, V. Kumar, T. P. Ma, P. Werner, E. Pippel, R. Sahoo, F. Damay, U. Rößler, C. Felser, and S. S. P. Parkin, "Magnetic antiskyrmions above room temperature in tetragonal Heusler materials," Nature **548**, 561 (2017).
[13]S. L. Zhang, G. van der Laan, and T. Hesjedal, "Direct experimental determination of the topological winding number of skyrmions in Cu_2OSeO_3," Nat. Commun. **8**, 14619 (2017).
[14]A. G. Kolesnikov, M. E. Stebliy, A. S. Samardak, and A. V. Ognev, "Skyrmionium–high velocity without the skyrmion Hall effect," Sci. Rep. **8**, 16966 (2018).
[15]L. Desplat, J.-V. Kim, and R. Stamps, "Paths to annihilation of first- and second-order (anti) skyrmions via (anti)meron nucleation on the frustrated square lattice," Phys. Rev. B **99**, 174409 (2019).
[16]S. Bera and S. S. Mandal, "Theory of the skyrmion, meron, antiskyrmion, and antimeron in chiral magnets," Phys. Rev. Res. **1**, 033109 (2019).
[17]L. Du, A. Yang, A. V. Zayats, and X. Yuan, "Deep-subwavelength features of photonic skyrmions in a confined electromagnetic field with orbital angular momentum," Nat. Phys. **15**, 650 (2019).
[18]J. Yang, X. Z. Zheng, J. F. Wang, Y. T. Pan, A. X. Zhang, T. J. Cui, and G. A. E. Vandenbosch, "Symmetry-protected spoof localized surface plasmonic skyrmion," Laser Photonics Rev. **16**, 2200007 (2022).
[19]H. Ge, X. Y. Xu, L. Liu, R. Xu, Z. K. Lin, S. Y. Yu, M. Bao, J. H. Jiang, M. H. Lu, and Y. F. Chen, "Observation of acoustic skyrmions," Phys. Rev. Lett. **127**, 144502 (2021).
[20]L. Cao, S. Wan, Y. Zeng, Y. Zhu, and B. Assouar, "Phononic skyrmions," arXiv:2209.12706 (2022).
[21]T. J. Davis, D. Janoschka, P. Dreher, B. Frank, F.-J. Meyer zu Heringdorf, and H. Giessen, "Ultrafast vector imaging of plasmonic skyrmion dynamics with deep subwavelength resolution," Science **368**, eaba6415 (2020).
[22]S. Tsesses, E. Ostrovsky, K. Cohen, B. Gjonaj, N. H. Lindner, and G. Bartal, "Optical skyrmion lattice in evanescent electromagnetic fields," Science **361**, 993 (2018).
[23]W. Lin, Y. Ota, Y. Arakawa, and S. Iwamoto, "Microcavity-based generation of full Poincaré beams with arbitrary skyrmion numbers," Phys. Rev. Res. **3**, 023055 (2021).
[24]Y. Dai, Z. Zhou, A. Ghosh, R. S. K. Mong, A. Kubo, C.-B. Huang, and H. Petek, "Plasmonic topological quasiparticle on the nanometre and femtosecond scales," Nature **588**, 616 (2020).
[25]X. R. Lei, A. P. Yang, P. Shi, Z. W. Xie, L. P. Du, A. V. Zayats, and X. C. Yuan, "Photonic spin lattices: Symmetry constraints for skyrmion and meron topologies," Phys. Rev. Lett. **127**, 237403 (2021).
[26]M. Król, H. Sigurdsson, K. Rechcińska, P. Oliwa, K. Tyszka, W. Bardyszewski, A. Opala, M. Matuszewski, P. Morawiak, R. Mazur, W. Piecek, P. Kula, P. G. Lagoudakis, B. Piętka, and J. Szczytko, "Observation of second-order meron polarization textures in optical microcavities," Optica **8**, 255 (2021).
[27]Y. Shen, E. C. Martínez, and C. Rosales-Guzmán, "Generation of optical skyrmions with tunable topological textures," ACS Photonics **9**, 296 (2022).
[28]Z. L. Deng, T. Shi, A. Krasnok, X. Li, and A. Alù, "Observation of localized magnetic plasmon skyrmions," Nat. Commun. **13**, 8 (2022).
[29]X. Li, L. Liu, Z. Zhou, J. Shen, Y. Zhang, G. Han, and Z. Li, "Highly sensitive and topologically robust multimode sensing on spoof plasmonic skyrmions," Adv. Opt. Mater. **10**, 2200331 (2022).
[30]R. D. Muelas-Hurtado, K. Volke-Sepúlveda, J. L. Ealo, F. Nori, M. A. Alonso, K. Y. Bliokh, and E. Brasselet, "Observation of polarization singularities and topological textures in sound waves," Phys. Rev. Lett. **129**, 204301 (2022).
[31]C. Shi, R. Zhao, Y. Long, S. Yang, Y. Wang, H. Chen, J. Ren, and X. Zhang, "Observation of acoustic spin," Natl. Sci. Rev. **6**, 707 (2019).
[32]Z. Gao, F. Gao, H. Y. Xu, Y. M. Zhang, and B. L. Zhang, "Localized spoof surface plasmons in textured open metal surfaces," Opt. Lett. **41**, 2181 (2016).
[33]E. Cubukcu and F. Capasso, "Optical nanorod antennas as dispersive one-dimensional Fabry–Pérot resonators for surface plasmons," Appl. Phys. Lett. **95**, 201101 (2009).
[34]N. Cselyuszka, M. Sečujski, N. Engheta, and V. Crnojević-Bengin, "Temperature-controlled acoustic surface waves," New J. Phys. **18**, 103006 (2016).